Supplementary Information for "Quantum oscillation of electron nonreciprocity in charge ordered 1*T*-$TiSe_2$"

S1. Methods

X-ray diffraction measurements of Synthesized 1T-TiSe2 Single Crystal

X-ray diffraction measurements were performed on the 1*T*-$TiSe_2$ single crystal using a custom-designed X-ray instrument equipped with a Mo Kα (17.48 keV) X-ray source. The bright and sharp Bragg peaks indicate the high crystalline quality of our sample (Fig. S1). The determined lattice parameters are $a = b = 3.549$ Å, $c = 5.999$ Å, $\alpha = \beta = 60°$, $\gamma = 120°$.

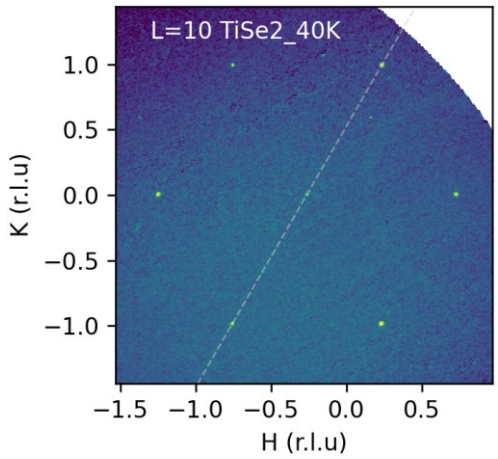

Figure S1. X-ray diffraction characterization of single crystal 1*T*-$TiSe_2$. Figure presents a (H, K) map of reciprocal space at L = 10 (L is reciprocal lattice unit for *c*-axis), measured at 40 K. The dashed line indicates the K direction.

Electrical transport measurements

Optical micrographs of the graphite-$TiSe_2$-Au and graphite-$TiSe_2$-graphite devices are presented in Fig.S2(a)&(b), respectively. For the AC+DC measurement in Fig.4, the DC bias was applied using a Keithley 2400 source meter with the setup showed in Fig.S2(c). With this configuration, a current bias $I = I_{\mathrm{AC}} \cos \omega t + I_{\mathrm{DC}}$ can be applied. Substituting the equation of nonreciprocal voltage response from the eMChA theory in the main text (Eq.(2)), we have:

$$\Delta V = \left(I_{\mathrm{DC}}^2 + \frac{1}{2} I_{\mathrm{AC}}^2 + 2 I_{\mathrm{DC}} I_{\mathrm{AC}} \cos \omega t + \frac{1}{2} I_{\mathrm{AC}}^2 \cos 2\omega t\right) \gamma B \cos \theta \qquad \text{(S1)}$$

That is to say, an AC current bias generates a second harmonic voltage (SHV), while a DC current bias has no influence to the SHV within the eMChA theory. Root-mean-square values

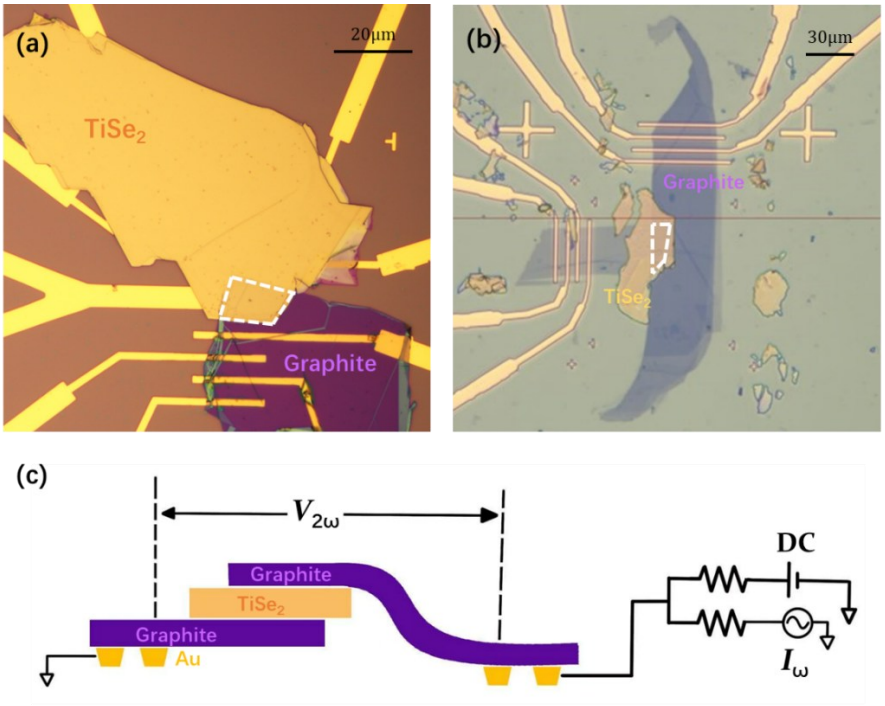

Figure S2. 1*T*-TiSe₂ heterostructure devices and measurement setup. (a), (b) Optical micrographs of (a) graphite-$TiSe_2$-Au and (b) graphite-$TiSe_2$-graphite devices. The overlapped regions of bottom graphite are outlined by white dashed polygons. (c) Schematic diagram of the AC+DC electrical measurement configuration. The AC and DC currents, each routed through a 1 MΩ resistor, are combined to form the (AC+DC) current bias.

are used in all AC measurements and data analysis ($I_{\mathrm{AC}} = \sqrt{2} I_{\omega}$), thus we have:

$$V_{2\omega} = \gamma B I_{\omega}^2 \cos\theta \tag{S2}$$

Substituting Eq.(3) into Eq.(S2), we have:

$$V_{2\omega}(B) = [\alpha(B)\sin(2\pi B/T_B + \varphi) + \beta(B)] I_{\omega}^2 \cos\theta \tag{S3}$$

To remove the background from the oscillating SHV signal, we took the second derivative of $V_{2\omega}$ with respect to B:

$$V''_{2\omega} = [-(2\pi/T_B)^2 \alpha \sin(2\pi B/T_B + \varphi) + 2(2\pi/T_B)\alpha' \cos(2\pi B/T_B + \varphi) + \alpha'' \sin(2\pi B/T_B + \varphi) + \beta''] I_{\omega}^2 \cos\theta \tag{S4}$$

We took an approximation that α' and β' are negligible compared to $\alpha 2\pi/T_B$, we have

$$V''_{2\omega}(B) T_B^2 \approx -\alpha(B) I_{\omega}^2 4\pi^2 \sin(2\pi B/T_B + \varphi) \tag{S5}$$

which is Eq.(4) in the main text.

S2. Ruling out other oscillation sources

In the main text, we reported prominent second-harmonic ($V_{2\omega}$) oscillation in graphite- $TiSe_2$-Au devices. This "antisymmetric" geometry raises the possibility that the observed non-reciprocity is an artifact of the device structure. Thus, using graphite as top and bottom contacts is necessary to identify the origin of the SHV oscillation. As shown in Fig.S3, graphite-$TiSe_2$-graphite symmetric devices (#2 and #3) exhibit *B*-periodic oscillation similar to that of the graphite-$TiSe_2$-Au asymmetric devices (#1, #4 and #5). This confirms that the *B*-periodic oscillation we observed is not originated from asymmetric contacts.

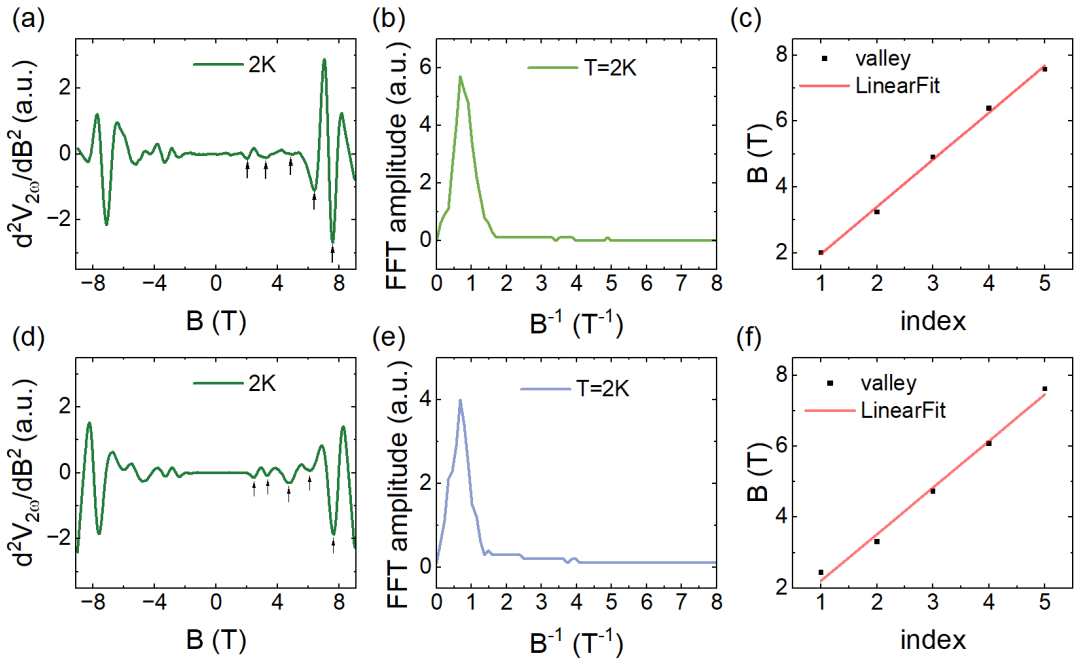

Figure S3. SHV oscillation in graphite-$TiSe_2$-graphite devices. (a) Second derivative of the SHV as a function of the magnetic field for device #2. *B*-periodic oscillation similar to those presented in the main text are shown. (b) Fast Fourier Transform (FFT) spectrum of the data showed in (a). The main peak in the FFT spectrum confirms the oscillation is *B*-periodic. (c) The magnetic field values of the valleys indicated by the black arrows in (a) versus their oscillation index. A linear relation is showed. (d)-(f) Results from device #3, following the same analysis in (a)-(c).

We also studied the graphite contribution to the SHV signal. As shown in Fig.S4(a), the SHV signal in a graphite-$TiSe_2$ device (measured in the configuration showed in Fig.1(b)) is

overwhelmingly larger than that in graphite. Besides the SHV signals, we measured the resistance (first-harmonic response) of device #1 and graphite using the same configuration in Fig.S4(a), which exhibits 1/*B*-periodic oscillation. This is confirmed by the linear relation of index vs 1/*B* demonstrated by the black squares line gray line in Fig.S4(c). We attribute this oscillation to the contact resistance at the $TiSe_2$-graphite interface. While sweeping the magnetic field perpendicular to the graphite thin flake, the Landau levels of graphite are periodically squeezed out of Fermi level, causing the contact resistance changes periodically. If the SHV oscillation was originated from the $TiSe_2$-graphite interface, we would except the oscillation show 1/*B*-periodicity. In Fig.S4(c), we plotted the extrema index of the SHV oscillation (red circles) versus their corresponding field values (in 1/*B*). A large deviation from linear relation can be seen. Taken together, these control experiments (Fig.S3, S4 and Fig.2(a)) conclude that the observed *B*-periodic SHV oscillation is originated from the 1*T*-$TiSe_2$ itself.

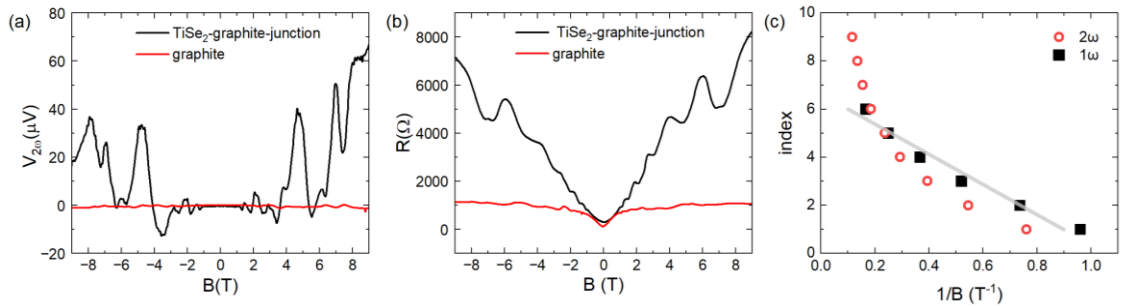

Figure S4. (a) The black curve is the raw SHV data measured in device#1 with the configuration showed in Fig.1(b), which is significantly higher than that in graphite. (b) The resistance measured by the same voltage probes in (a). (c) The valley index of the SHV and first-harmonic magnetoresistance oscillations versus the inverse of their magnetic fields, labeled by red circles and black squares, respectively. Grey line is the linear fit of the black square data points. The valley index of the SHV does not follow the 1/B functional form.

Comparing the SHV oscillation between devices with different 1*T*-$TiSe_2$ thickness also provide information about the origin of the oscillation. According to Eq.(4) in the main text, the oscillation amplitudes need to by normalized by multiplying the amplitude by the square of the oscillation period. We plotted a scatter diagram of the normalized amplitude versus thickness of 1*T*-$TiSe_2$ for 5 devices (Fig S5(a)). The result demonstrates that the oscillation amplitudes decrease with increasing 1*T*-$TiSe_2$ thickness, excluding the possibility that the SHV oscillation is originate from $TiSe_2$-graphite contact resistance. Meanwhile, we also presented a plot of oscillation period versus 1*T*-$TiSe_2$ thickness (Fig S5(b)), showing no

obvious thickness dependence.

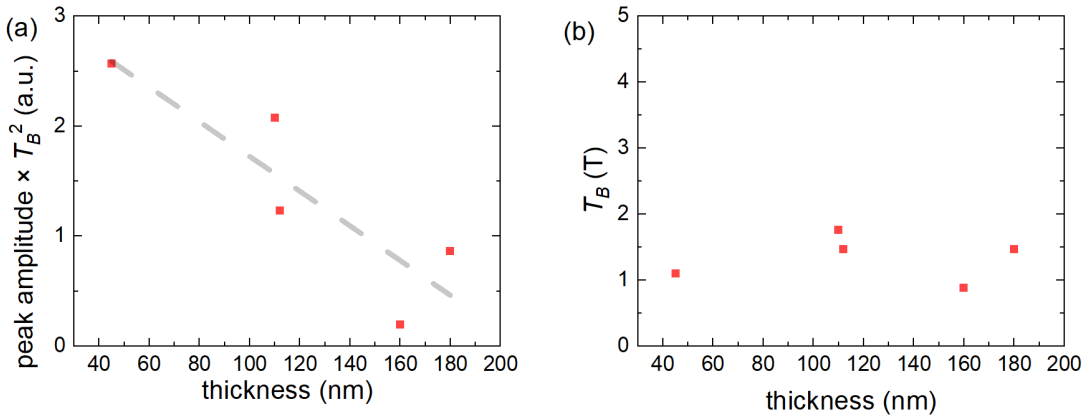

Figure S5. Thickness dependence of the FFT amplitude. (a) FFT amplitudes of the oscillation as a function of 1*T*-$TiSe_2$ thickness for 5 devices. The FFT amplitudes are normalized by multiplying them by the square of their oscillation period (T_B^2). The plot clearly demonstrates that the oscillation amplitude decreases with increasing thickness. **(b)** SHV oscillation period as a function of 1*T*-$TiSe_2$ thickness for 5 devices. No thickness dependence of the oscillation period is observed.

S3. Supplementary data from other devices

In Fig.2, we demonstrated that the oscillation period is solely related to the out-of-plane component of magnetic field. Here we present the SHV oscillation with tilting magnetic field of other four devices (Fig S6), which exhibit similar properties. Fig.3(c)(f) summarized the relation of oscillation amplitude versus temperature or excitation current in different devices. Here we present the original data, see Figs.S7&S8. Fig.4(c) in the main text showed the π phase shift driven by DC current bias. We present the original data and examples for the phase shift $\Delta\varphi$ extraction in Fig.S9. In Fig.S9(d)-(f), we plotted the $V''_{2\omega}$ minima or maxima magnetic field positions versus their indexes (integers for minima and half integers for maxima). The oscillation phase φ can be extracted from the *x*-intercept c_0 by $\varphi = 2\pi(c_0 - 3/4 + n)$, where n is an integer to ensure that $0 \leq \varphi < 2\pi$. The two fitting lines for device #3 are not parallel to each other. This may be caused by the inaccuracy of the index values, which may be plagued by a missing extreme point at around $B = 5$ T in $V''_{2\omega}(B)$ curves for positive DC biases.

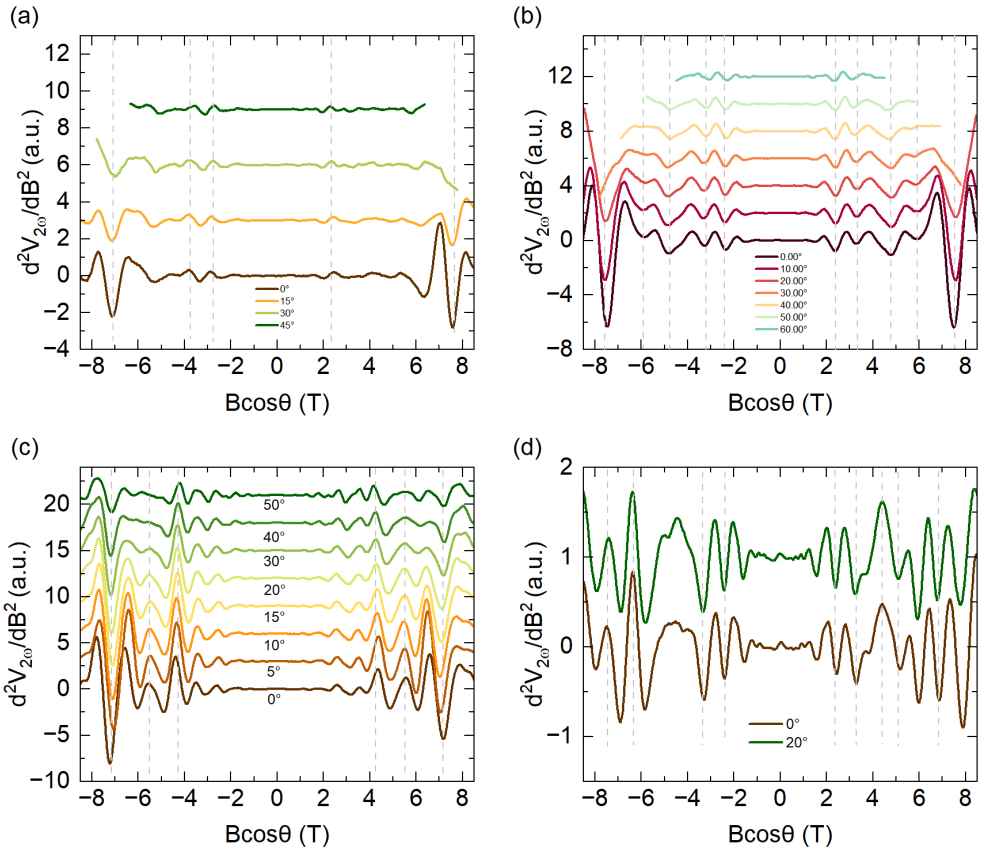

Figure S6. Magnetic field angle dependence of SHV oscillation for device #2, #3, #4, and #5. Second derivative of SHVs with different magnetic field tilting angles (the definition of θ is same as Fig.2) are plotted as a function of the out-of-plane magnetic field component ($B\cos\theta$). Offsets were added for clarity. The grey dashed lines track the positions of the oscillation extrema. The vertical alignment of these extrema across all angles confirms that the oscillatory behavior depends solely on the out-of-plane component of the magnetic field. Subfigures (a)-(d) correspond to devices #2, #3, #4 and #5, respectively. Measurements were conducted at $T = 2$ K with $I_{ex} = 1$ μA.

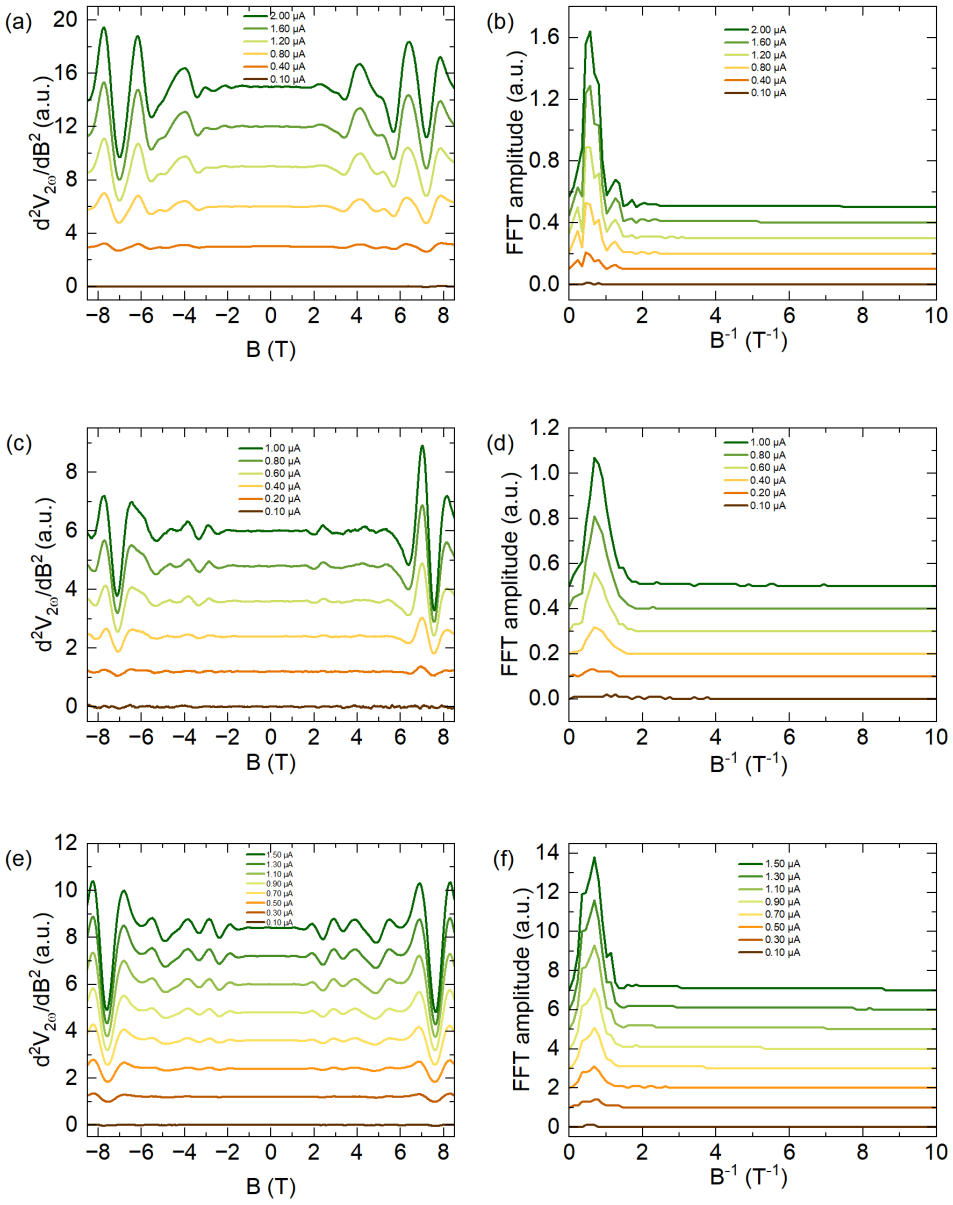

Figure S7. Excitation current dependence of SHV oscillation for device #2, #3, and #4. (a) A stacked plot of the second derivative of SHVs as a function of magnetic field for device #2, measured at various AC excitation currents. A clear trend is observed where the oscillation amplitude strengthens as the excitation current increases. (b) Corresponding FFT spectra for the data presented in (a). (c), (d) and (e), (f) The corresponding stacked plot and FFT spectra for device #3 and device #4, respectively. Offsets were added for clarity in all subfigures. Measurements were conducted at $T = 2$ K and $\theta = 0°$.

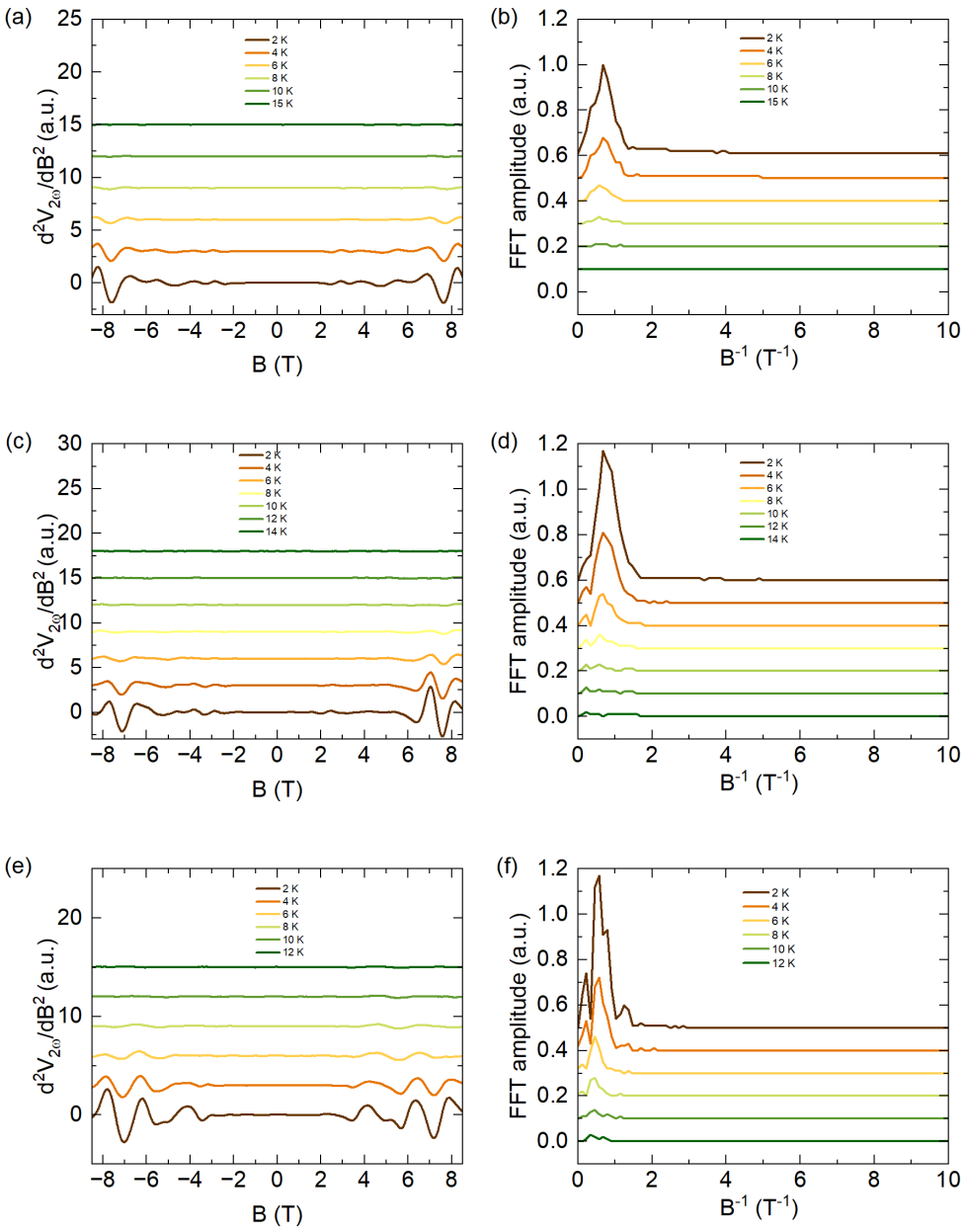

Figure S8. Temperature dependence of SHV oscillation for device#2 #3 #4. (a) A stacked plot of the second derivative of SHVs as a function of magnetic field for device #2, measured at various temperatures. The oscillation diminish as the temperature increases. (b) Corresponding FFT spectra for the data presented in (a). (c), (d) The corresponding stacked plot and FFT spectrum for device #3. (e), (f) The corresponding stacked plot and FFT spectrum for device #4. Offsets were added for clarity in all subfigures. Measurements were conducted with $I_{ex} = 1\ \mu A$ and $\theta = 0°$.

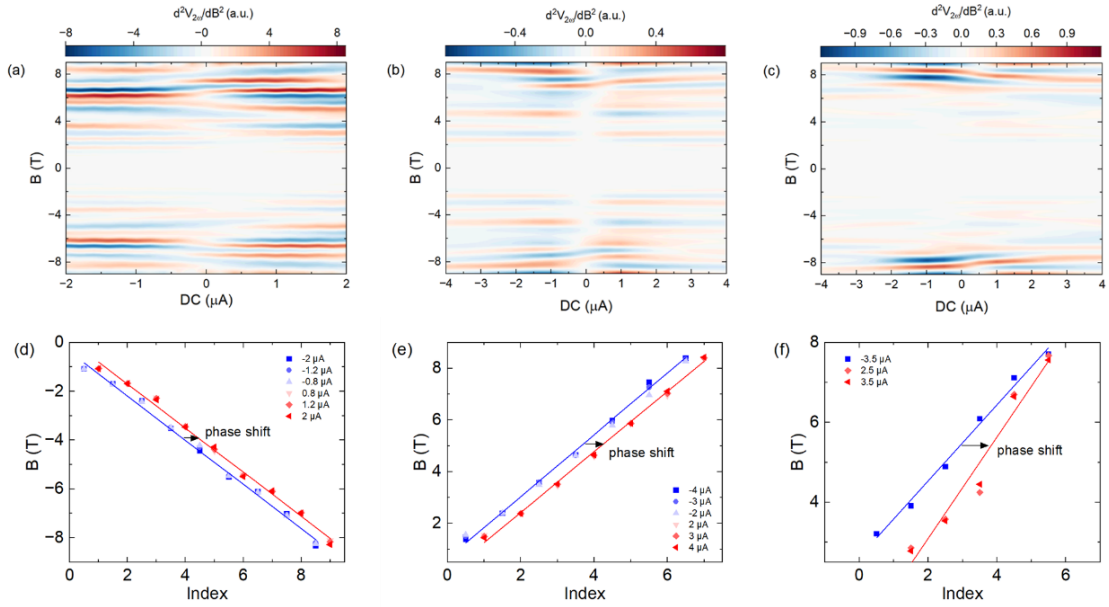

Figure S9. DC current bias dependence for devices #1, #2, and #3. (a) A 2D contour plot of the second derivative of SHV for device #1 as a function of DC excitation current and magnetic field. (d) Linear fits of the magnetic field at the oscillation valley in (a) versus oscillation index. The intercept of the fitted line on the *x*-axis (which can be regard as the oscillation phase) shifts when the DC current bias changed from positive to negative. (b), (e) The corresponding 2D contour plot and phase analysis for device #2. (c), (f) The corresponding 2D contour plot and phase analysis for device #3. Measurements were conducted with $I_{\mathrm{AC}} = 1\ \mu\mathrm{A}$, $T = 2\ \mathrm{K}$ and $\theta = 0°$.

S4. Tight-Binding Model for Chiral CDW Domain Wall

To demonstrate the presence of edge states, we derive an ab initio tight-binding model for a CDW domain wall. Consider the schematic setup shown in Fig. S10(a). The left and the right regions correspond to domains with opposite CDW chirality, and the middle region corresponds to the domain wall. The Hamiltonian for the whole system can be expressed as

$$H = \begin{bmatrix} h_L & T_L & 0 \\ T_L^\dagger & h_{DW} & T_R \\ 0 & T_R^\dagger & h_R \end{bmatrix} \quad (1)$$

Here, $h_{L/R}$ represents half-infinite Hamiltonian of the chiral CDW phase with different chirality, connected by inversion symmetry. h_{DW} is the Hamiltonian of the domain wall region with an intercell coupling$t_{\mu\nu} = te^{-|r_{\mu\nu}|/a}$, and T_R (T_L) represents coupling between the $h_R(h_L)$ and h_{DW}, where $t = 50meV$, and μ, ν are orbital indexes. Then, Green's function of the chiral CDW domain wall can be determined as

$$G_{DW}(\varepsilon) = (\varepsilon - h_{DW} - \Sigma_L - \Sigma_R)^{-1} \quad (2)$$

where the self-energy$\Sigma_{L/R} = T_{L/R} G_{L/R} T_{L/R}^\dagger$, with $G_{L/R}$ being Green's function for the half-infinite system with chiral CDW. The calculated spectral function $A_{DW}(\varepsilon) = \frac{1}{\pi}\mathrm{ImTr}G_{DW}(\varepsilon - i0^+)$ for the chiral CDW domain wall is displayed in Fig.S10(b). One can indeed see domain wall modes located inside the bulk gap, which has dispersion along the vertical c direction. Given the insulating behavior of the bulk chiral CDW state in low-temperature setup, these in-gap domain wall modes are expected to play a role in the vertical transport observed in our experiment.

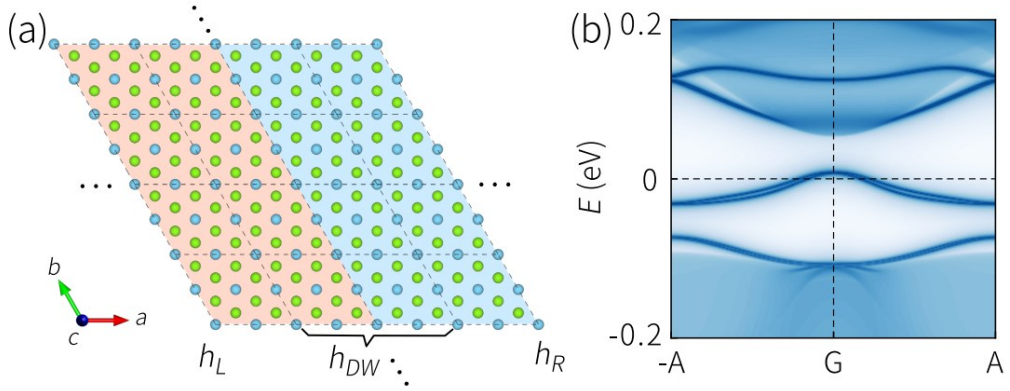

Figure S10. The in-gap domain wall modes calculation. (a) Top view of the chiral CDW domain wall. Red and blue regions indicate the chirality. The 2 × 2 × 2 supercell is highlighted with dashed lines. **(b)** Plot of spectral function of the chiral CDW domain wall along the vertical direction.